CONFERENCE PRE-PRINT

LOWER DENSITY LIMIT FOR ACCESSING TO ELM SUPPRESSION USING $N = 4$ RMP IN EAST

X.M. Wu[1,2], Y. Sun[1*], Q. Ma[1], S. Gu[1], M. Jia[1], Y.Q. Liu[3], Y.F. Wang[1], C. Ye[4], P. Xie[1], A. Loarte[5], P.B. Snyder[6], X.X. Zhang[1], K.N.Geng[1], Y. Liang[7], C. A. Paz-Soldan[8], G.Q. Li[1], J. Qian[1], L. Zeng[9], Q. Zang[1], Y.Y. Li[10], T. Zhang[1] and B. Wan[1]

1) Institute of Plasma Physics, Hefei Institutes of Physical Science, Chinese Academy of Sciences, Hefei 230031, China
2) University of Science and Technology of China, Hefei 230026, China
3) General Atomics, PO Box 85608, San Diego, CA 921865608, USA
4) School of Mechanical and Electrical Engineering, Chizhou University, Chizhou 247100, China
5) ITER Organization, Route de Vinon sur Verdon, 13115 St Paul Lez Durance, France
6) Oak Ridge National Laboratory, Oak Ridge TN, USA
7) Forschungszentrum Jülich, Jülich 52425, Germany
8) Columbia University, New York, NY 10027, USA
9) Department of Engineering Physics, Tsinghua University, Beijing 100084, China
10) Enn Science and Technology Development Co., Ltd, Langfang, China

*Email: ywsun@ipp.ac.cn

Abstract

Existence of operational window in both edge safety factor (q_{95}) and line averaged plasma density ($\langle n_e \rangle$) for suppression of Edge Localized Modes (ELMs) using $n = 4$ Resonant Magnetic Perturbations (RMPs) in low input torque plasmas has been observed in EAST experiment, in which q_{95} and plasma normalized beta (β_N) close to that required in ITER high-Q operation. Here, n is toroidal mode number of the magnetic perturbation. Different from previous observations in the other machines, there is not only an upper density limit but also a lower one for accessing to ELM suppression. Modelling results using the MARS-F code show that RMP with linear plasma response has a peak at intermediate plasma density and decays in both sides with increasing and decreasing density, which results in a minimal RMP field penetration threshold at intermediate plasma density. In this experiment, different densities result in different edge current profiles, which changes the eigenmode structure that causes a reduction of resonant field in both low and high density cases and hence makes field penetration be more difficult. The modelled window of strongest resonant plasma response in terms of [$\langle n_e \rangle$, q_{95}] agrees well with the observations of ELM suppression in EAST. Peeling-ballooning stability analysis using the ELITE code shows that plasmas gradually approach peeling stability boundary caused by increase of edge bootstrap current as the plasma density decreases, which is consistent with the observation that ELMs come back again in lower density plasmas for fixed q_{95}. These findings indicate that linear modelling with full toroidal geometry can well predict the optimized RMPs for accessing to ELM suppression and reveals the important roles of pedestal current on ELM suppression, which need to be carefully considered in the application of high n RMPs for ELM suppression in future ITER.

1 INTRODUCTION

Resonant magnetic perturbations (RMPs) have been demonstrated in multiple devices [1–4] as an effective method for suppression of type-I edge localized modes (ELM), which pose a risk of damage to the plasma facing materials in future ITER and other tokamak fusion reactors[5, 6]. However, it is still challenge to achieve RMP ELM suppression even with strong enough resonant fields [7, 8] especially in low input torque plasmas [9, 10]. Understanding operational window for accessing to ELM suppression using RMP is critical for extrapolating present results to future ITER so that type-I ELMs can be reliably controlled.

RMP ELM suppression is often strongly sensitive to edge safety factor q_{95} [11–14], because the resonant condition depends on the alignment of RMP field structure and the edge field line pitch, i.e. the RMP spectrum effect [15–19]. Plasma density has also been identified as a critical factor influencing RMP ELM suppression in multiple devices [14, 20–22]. Early experiments

on DIII-D showed that ELMs cannot be suppressed when the density at the pedestal top exceeds a certain threshold [20]. Similarly, ELM control experiments on ASDEX-Upgrade demonstrated that both plasma edge density and temperature must remain below critical values to achieve ELM suppression [21]. Subsequent experiments and modelling on DIII-D indicated that a sufficiently low plasma density is essential for the penetration of pedestal top RMP harmonics that led to ELM suppression [22–24]. The threshold density was also observed to be affected by plasma configuration [10]. Nonlinear bifurcation modelling of RMP-induced ELM suppression also confirms the existence of an upper density limit for suppression, which varies with electron temperature and is strongly influenced by electron fluid resonance [25], a finding consistent with experimental results from both DIII-D and ASDEX-Upgrade.

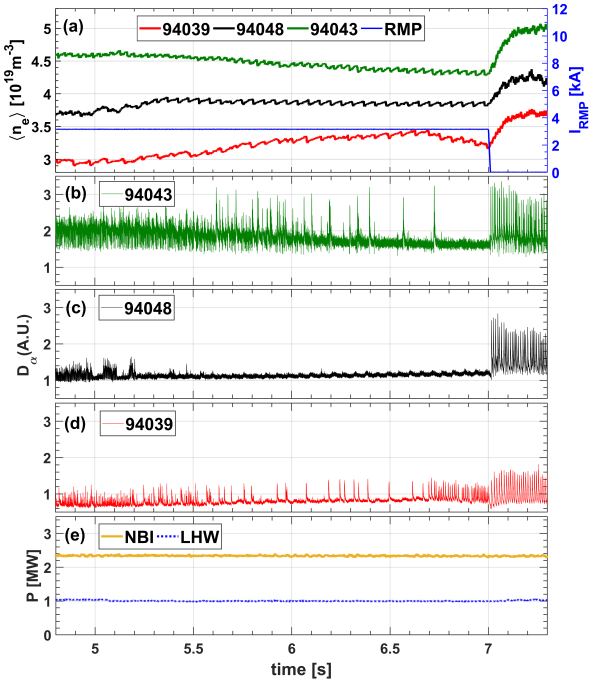

FIG. 1. Temporal evolution of (a) the line-averaged density and RMP coil current (blue line), (b)–(d) D_α signals, and (e) the heating power for three discharges with different densities 94039(red line), 94048(black line) and 94043(green).

Existence of both upper and lower density limits for ELM suppression using $n = 4$ RMPs has been observed in the EAST tokamak [14]. In this experiment, ELM suppression has been achieved in the line averaged plasma density range $\langle n_e \rangle \in [3.3, 4.4] \times 10^{19} m^{-3}$ (or $\in [0.44-0.6] n_{\rm GW}$, where $n_{\rm GW}$ is the Greenwald density limit), and the corresponding pedestal top density range is $n_{e,ped} \in [2.5, 3.5] \times 10^{19} m^{-3}$ (or $\in [0.33-0.47] n_{\rm GW}$). The corresponding pedestal electron collisionality range is $\nu_{*e,ped} \sim 0.35$–0.55. This density window is observed in the experiments employing both density-scan shot by shot and slow density ramp in one discharge using feed-forward gas puffing. Similar window effect also has been observed in the experiment using pellet injection or gas fueling for divertor flux control in EAST [26].

Examples of three discharges on RMP ELM suppression with different line-averaged densities is shown in Fig. 1. In this experiment, it has $B_T \sim 1.6$T, $q_{95} \sim 3.65$, $\beta_N \sim 1.45 - 1.6$, and neutral beam injection (NBI) torque $T_{\rm NBI} \sim 0.75$ Nm, which is lower than the equivalent one for 33MW NBI in ITER. Here, the auxiliary heating includes 1.8 MW co-current NBI, 0.5 MW counter-current NBI, and 1 MW lower hybrid wave (LHW). They all kept constant in the three discharges. Optimal ELM suppression is achieved at intermediate line averaged plasma density

EAST has achieved type-I ELM suppression with $n = 4$ RMPs in the plasmas with q_{95}, the normalized beta (β_N), and the input torque are close to that required in ITER high-Q operational scenario [14]. The advantage of using $n = 4$ RMPs is that it has negligible influence on energy confinement during RMP ELM suppression in EAST compared to that using low n RMPs [26]. This supports the use of high n RMPs for ELM suppression in ITER [27]. In this experiment, existence of operational windows in both q_{95} and line averaged plasma density ($\langle n_e \rangle$) for ELM suppression has been observed [14]. Different from previous observations in the other machines, there is not only an upper density limit but also a lower one for accessing to ELM suppression. This contradicts to previous understanding that lower density is favorable for field penetration that led to easier ELM suppression.

In this paper, the modeling of plasma response and peeling-ballooning mode (PBM) stability have been performed for different densities to understand the existence of operational window, especially the lower density threshold, for accessing to RMP ELM suppression observed in the EAST experiment.

2 OBSERVATION OF ELM SUPPRESSION DENSITY WINDOW IN EAST

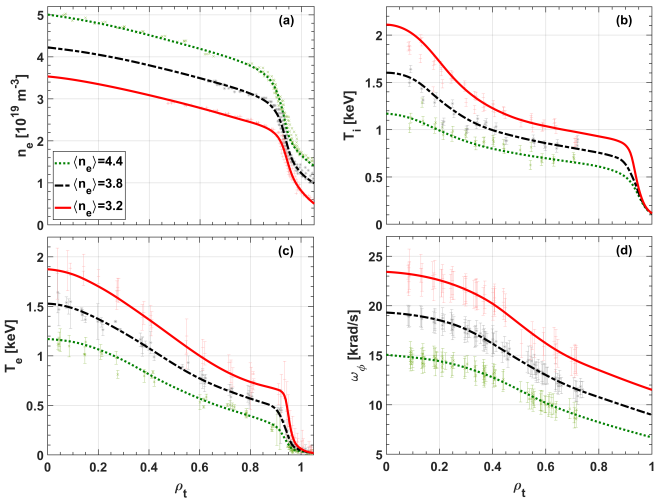

FIG. 2. Electron density (a), ion temperature (b), electron temperature (c), and toroidal rotation (d) profiles at different densities $\langle n_e \rangle = 3.2 \times 10^{19} m^{-3}$ (red line), $3.8 \times 10^{19} m^{-3}$ (black line) and $4.4 \times 10^{19} m^{-3}$ (green line). The scatter points represent measured data, and the curves are fitted profiles.

around $\langle n_e \rangle \sim 3.8 \times 10^{19} m^{-3}$ in discharge 94048, in which reliable ELM suppression was achieved start at $t = 5.2$s till the switch off of RMP at $t = 7$s. ELM suppression is less effective in both high and low density cases.

Kinetic profiles of electron density, ion and electron temperature, and toroidal angular rotation near $t = 6$s for the three discharges are shown in Fig. 2. Here, electron density is fitted from the measured one using reflectometer (scatter points in the figure) [28] with the constraints from the line-averaged densities measured by the POINT (PolarimeterINTerferometer) diagnostic[29]. The electron temperature, ion temperature, and toroidal rotation profiles were fitted from the measurements by Thomson scattering (TS)[30] and charge exchange recombination spectroscopy (CXRS)[31]. The resolution in pedestal density measurement is relatively good. Unfortunately, limited by the diagnostic capability, there are some uncertainties in temperature pedestal profiles in this experiment. Ion temperature and toroidal rotation measurement cannot cover the pedestal region. Therefore, only the variation of pedestal top temperature is considered in the fitting of temperature profiles. It is shown that the whole edge electron density steps down and pedestal top temperature steps up with decreasing line averaged density.

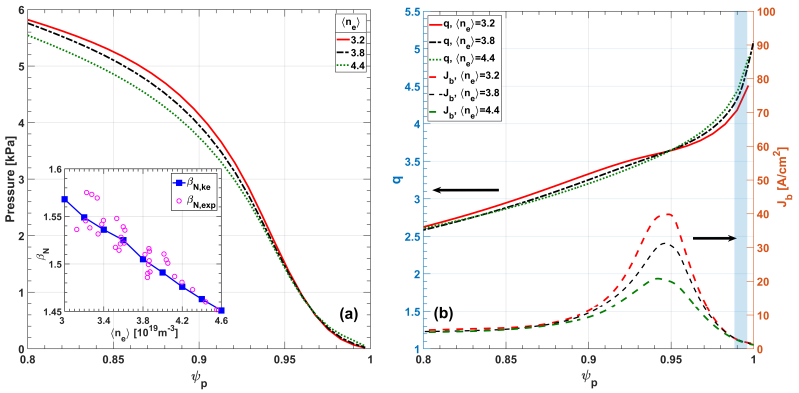

FIG. 3. The (a) pressure pedestal and (b) safety factor and bootstrap current distributions from reconstructed kinetic equilibria at different densities $\langle n_e \rangle = 3.2 \times 10^{19} m^{-3}$ (red line), $3.8 \times 10^{19} m^{-3}$ (black line) and $4.4 \times 10^{19} m^{-3}$ (green line). The inset in (a) shows the dependence of normalized beta on density from the kinetic equilibria (blue dotted line) compared to the experimental measurements (magenta circles).

To understand the density window effect, kinetic equilibria were reconstructed using the k-EFIT code [32, 33] based on magnetic measurements and kinetic profiles mentioned above. Pressure and safety factor of the reconstructed equilibria together with the modeled edge bootstrap current are shown in Fig. 3. Here, the pressure includes both thermal and fast ion pressure, which was calculated by the NUBEAM code [34], while the bootstrap current was calculated using the Sauter's model [35, 36]. To study the independent density effect, a series of kinetic equilibria at different densities were reconstructed with fixed $q_{95} = 3.65$ and total toroidal plasma current. In this experiment, lower density corresponds to higher pressure and normalized beta as shown in Fig. 3 (a). The density dependence of the normalized beta of the reconstructed kinetic equilibria agrees well with experimental observations, which indicates the reconstructed equilibria are reasonable. It is shown in Fig. 3 (b) that the safety factor in the pedestal steep gradient region becomes more flattened in lower density case because of a higher edge bootstrap current. This edge localized difference in q profile may result in different plasma response and the PBM stability.

3 MODELING OF PLASMA RESPONSE FOR UNDERSTANDING OF DENSITY WINDOW FOR ELM SUPPRESSION

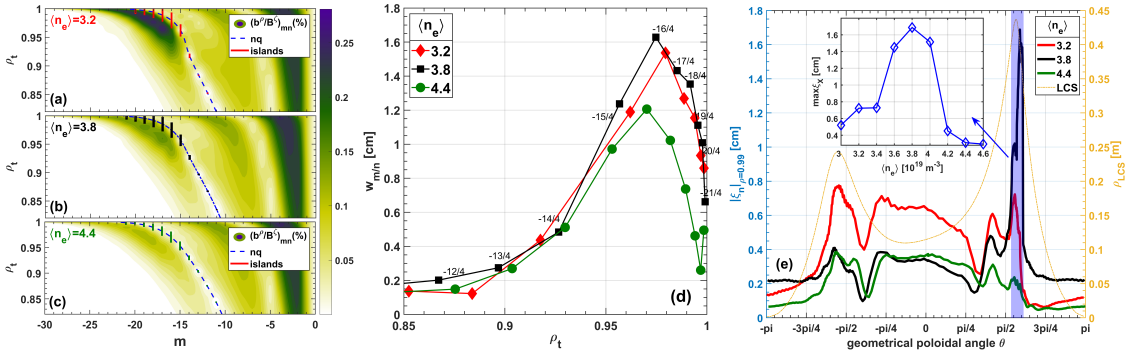

FIG. 4. Modeled (a-c) RMP spectrum, (d) edge magnetic island width, (e) poloidal distribution of boundary displacement at normalized radius $\rho = 0.99$ taking into account plasma response for three different densities $\langle n_e \rangle = 3.2 \times 10^{19} m^{-3}$ (red line), $3.8 \times 10^{19} m^{-3}$ (black line) and $4.4 \times 10^{19} m^{-3}$ (green line) using the MARS-F code. The subplot in (e) quantifies the dependence of maximum displacement near the X-point (light blue area) on density.

MARS-F code [37] has been employed for modeling linear plasma response for understanding this density window effects for accessing to ELM suppression with $n = 4$ RMPs. The resonant and non-resonant components of magnetic perturbations, and edge displacement at different densities taking into account plasma response are shown in figure 4. The dependence of response RMP spectrum on plasma density is shown in Fig. 4(a-c). It is shown that the non-resonant kink response (non-

resonant respect to field line pitch but resonant respect to kink mode pitch with poloidal mode number m slightly higher than the resonant harmonic at each surface) increases with decreasing plasma density, which is caused by the higher β_N as well as pedestal pressure gradient and current at lower density. The response of resonant harmonics are more complicate, since it depends on not only the global alignment of the perturbation field but also the local layer physics at the rational surfaces [38]. It is shown in Fig. 4(d) that the edge resonant components indicated by the magnetic island widths are larger at intermediate density ($\langle n_e \rangle = 3.8 \times 10^{19} m^{-3}$) than those at both higher ($\langle n_e \rangle = 4.4 \times 10^{19} m^{-3}$) and lower ($\langle n_e \rangle = 3.2 \times 10^{19} m^{-3}$) density cases. The dependence of poloidal distribution of edge plasma displacement shown in Fig. 4(e) gives the same result. The low-field-side mid-plane displacement ξ_M is the highest at lowest density, which means that the kink response is the strongest at the lowest density. Meanwhile, the X-point displacement ξ_X reaches maximum at intermediate plasma density at around $\langle n_e \rangle = 3.8 \times 10^{19} m^{-3}$ indicating strong peeling-like resonant response. This is consistent with the resonant field dependence in Fig. 4(a). This indicates that the ELM suppression links to the strength of edge resonant harmonics taking into account plasma response, which is also consistent with previous understanding based on linear modeling [16–18].

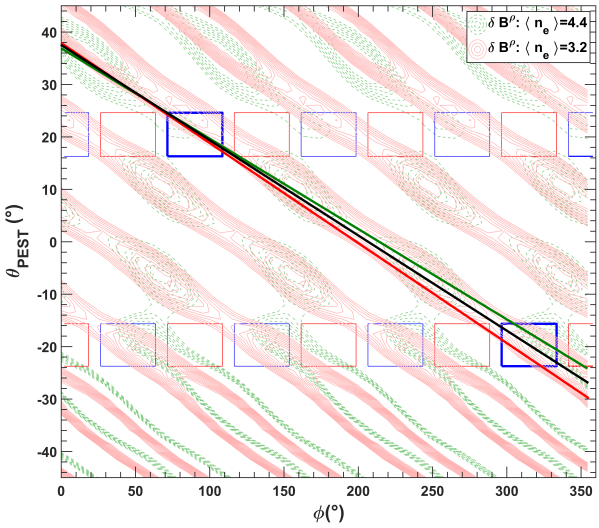

FIG. 5. The alignment of the applied odd parity $n = 4$ RMP field configuration with the edge eigenmode structure indicated by contour lines of δB^ρ taking into account plasma response at the normalized radius $\rho = 0.99$ at $\langle n_e \rangle = 3.0 \times 10^{19} m^{-3}$ (red) and $4.6 \times 10^{19} m^{-3}$ (green).

To understand why the strongest resonance happens at the intermediate density, the alignment of the applied odd parity $n = 4$ RMP field configuration with the edge eigenmode structure indicated by contour lines of δB^ρ taking into account plasma response at the normalized radius $\rho = 0.99$ at $\langle n_e \rangle = 3.2 \times 10^{19} m^{-3}$ (red) and $4.4 \times 10^{19} m^{-3}$ (green) is shown in Fig. 5. The colored squares indicates the mapping positions of the RMP coils (that vacuum perturbed field on this surface peaked at each coil's center), and hence, the color of them indicates the orientation of the normal component of the local perturbed field near the coils for an odd parity $n = 4$ RMP coil configuration. The colored lines in the figure are parallel to the corresponding mode pitches indicated by the colored contours of δB^ρ. To avoid too busy in the figure, the contours for the black line with intermediate density is neglected. The three lines are aligned to cross the center of one upper blue coil. If it crosses also one of the lower blue coil, it means good alignment with the applied field. It is shown that both the high ($4.4 \times 10^{19} m^{-3}$) and low ($\langle n_e \rangle = 3.2 \times 10^{19} m^{-3}$) densities ones missed good alignment (start to cross one of the red lower coils, and their toroidal shifts are around a half width of one coil) with the odd $n = 4$ RMP configuration in opposite directions, while the black one with intermediate density ($\langle n_e \rangle = 3.8 \times 10^{19} m^{-3}$) aligns well with the applied field. This means again that the strongest edge resonance taking into plasma response favors to accessing to ELM suppression, similar to those reported in previous studies [39–41]. The only difference here is that the local change of the edge current profiles due to density change in this experiment is large enough to change the pitch angle of edge mode structure and its resonance with the applied field. This means that the resonant condition for $n = 4$ RMP ELM suppression is also sensitive to pedestal kinetic profiles.

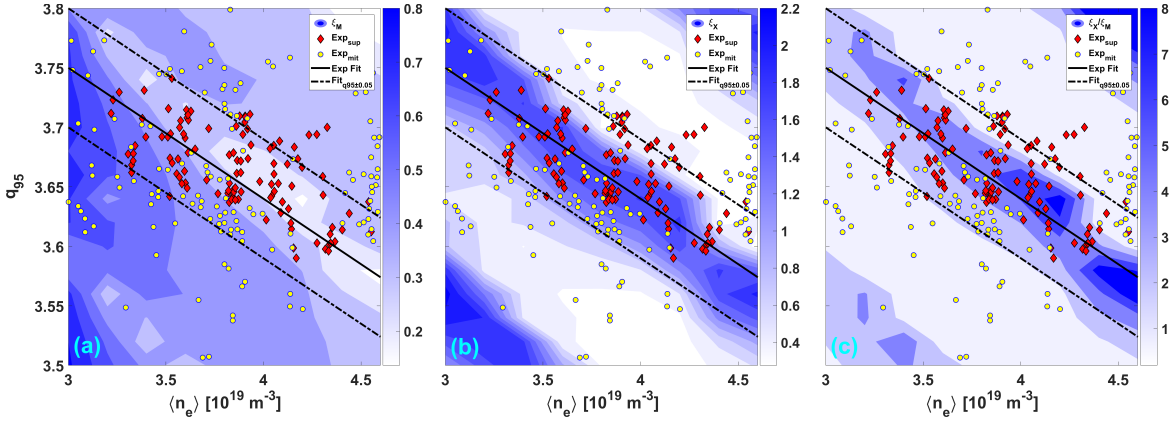

FIG. 6. Operational space of experimentally observed ELM suppression (red diamonds) and ELM mitigation (yellow circles) in [q_{95}, $\langle n_e \rangle$] domain superimposed on colored contour plots of plasma response in boundary displacement at low-field-side mid-plane ξ_M (a) and near the X-point ξ_X (b), and their ratio ξ_X/ξ_M (c). The solid black line is fitted from the ELM suppression data, together with dashed lines showing banded q_{95} window with a width $\delta q_{95} = \pm 0.05$.

To give a global picture of ELM suppression window in the domain [n_e, q_{95}], the correlation between ELM suppression

and linear plasma response in radial displacement near low-field-side mid-plane ξ_M, near the X-point ξ_X, and their ratio ξ_X/ξ_M are shown in Fig. 6 (a-c), respectively. They show a clear dependence on both plasma density and q_{95}. The resonant q_{95} window changes with plasma density, while the width of q_{95} window for ELM suppression is almost constant at different plasma density. It is shown that strongest resonant plasma response indicated by the strength of ξ_X, and ξ_X/ξ_M has a narrow mountain ridge in the [n_e, q_{95}] domain, which aligns well with the domain that observed ELM suppression using $n = 4$ RMPs in EAST. On the contrary, the ELM suppression cases are located at the valley of non-resonant kink plasma response. This means ELM suppression is closely related to peeling-tearing type resonant plasma response. In fixed $q_{95} = 3.65$ cases shown in Fig. 6 (c), the linear plasma response at intermediate density exhibits the strongest resonance, which makes it easier to penetrate at this density. Both high and low densities are unfavorable for RMP field penetration.

The loss of ELM suppression at low density with fixed q_{95} because resonant q_{95} window shifted upwards as density decreases, which is caused by change of eigenmode structure due to changes of edge pressure and bootstrap current profiles as discussed above. This is different from previous understanding of density dependence based on resistive layer physics in the studies of density scaling for field penetration threshold [23]. The high-density limit observed here is also not due to higher penetration threshold but due to shift of resonant response window. The shift of suppression window suggests linear plasma response to high-n RMPs is very sensitive to kinetic profiles especially edge current profile, although q_{95} is fixed. This explains why we observed both upper and lower density limits for accessing to ELM suppression in this experiment.

This result also means that the optimal q_{95} for ELM suppression changes with plasma density. Therefore, for ELM control using high-n RMP, one has to carefully control q_{95} in the experiment to keep the resonant condition, when plasma pedestal kinetic profiles are changed as the density scan in this experiment.

4 IMPACT OF PLASMA DENSITY ON PBM STABILITY DURING $N = 4$ RMP ELM CONTROL

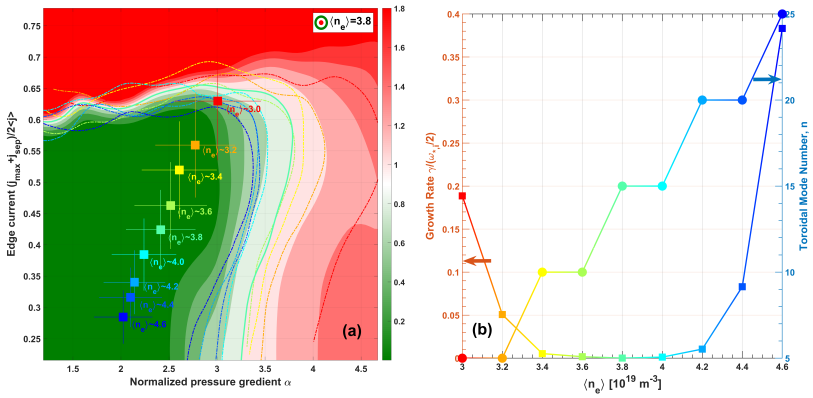

FIG. 7. (a) Stability boundaries (colored curves) and operational points (scatter points) at various densities superimposed on the contour plot of PBMs growth rate at $\langle n_e \rangle = 3.8 \times 10^{19} m^{-3}$, and (b) the density dependence of the PBM growth rate (squares) and the dominant toroidal mode number (circles).

To check the consistence between pedestal stability changes and ELM control effects at different phases, ELITE code [42–44] is employed to model the pedestal stability. Previous study [45] indicates that the dominant modes in this type-I ELMy H-mode without RMP are low-n peeling-ballooning modes (PBMs), which growth rates are significantly reduced after the application of RMPs, especially during the phase with RMP ELM suppression. The stabilization effect mainly comes from the reduction of pedestal bootstrap current after the application of RMPs.

To understand the density window effects, density dependence of operational regimes and growth rates of PBMs are shown in Fig. 7. Fig. 7(a) displays the stability boundaries (curves of different colors) and the locations of the experimental equilibria (scattered points of different colors). The background color represents the growth rate contour for the intermediate density case. It is shown that plasmas shifts from the ballooning modes dominant regime towards peeling stability boundary caused by increase of edge bootstrap current as the plasma density decreases, which is consistent with the observation that ELMs come back again in low density plasmas for fixed q_{95}. Fig. 7(b) presents the eigenmode growth rates and the dominant toroidal mode numbers for different densities. It clearly shows that both high- and low-density

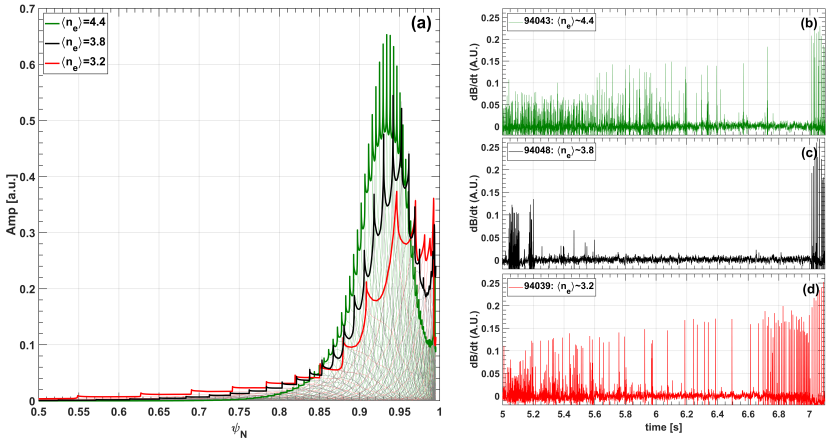

FIG. 8. The eigenmode structure (a) and Mirnov signals at high-field-side mid-plane (b) at different densities in the three discharges shown in Fig. 1.

cases exhibit large growth rates. The dominant toroidal mode number also indicates the characteristics PBMs at different densities. Intermediate density lies in the most stable region against PBMs, which also consists with that optimal ELM suppression only achieved at intermediate plasma density.

Figure 8(a) shows the modeled eigenmode structures corresponding to the three different densities. It is shown that the eigenmode is mainly localized at the pedestal steep gradient region indicating that ballooning modes dominant at high density, while it is localized at the pedestal foot indicating that peeling modes dominant at low density. This is consistent with the results shown in Fig. 7. Figures 8(b)–(d) show the evolution of Mirnov signals ($\frac{\mathrm{d}B}{\mathrm{d}t}$) indicating ELM crash amplitude at different densities. Since the spikes in Mirnov signal are caused by the response of equilibrium control system to the fast change of stored energy $\frac{\mathrm{d}W}{\mathrm{d}t}$ due to ELM crash, it has $\frac{\mathrm{d}B}{\mathrm{d}t} \propto \frac{\mathrm{d}W}{\mathrm{d}t}$. Therefore, it is a better indicator for ELM size than that of the D_α signal in Fig. 1. It is shown that the observed mitigated ELM crash has larger amplitudes at lower density, which is qualitatively consistent with the modeled difference in growth rates in Fig. 7. This confirms the trends of modeling results on the changes of PBMs' stability.

5 SUMMARY AND CONCLUSION

In summary, modeling of plasma response using the MARS-F code and peeling-ballooning stability using the ELITE code well explained the reason why ELM suppression by $n = 4$ RMPs has both upper and lower density limits. The changes of pedestal bootstrap current resulted from density change play the key role in determining both plasma response to RMPs and stability of peeling-ballooning modes.

Existence of operational window in both edge safety factor (q_{95}) and line averaged plasma density for suppression of ELMs using $n = 4$ RMPs in low input torque plasmas has been observed in EAST experiment, in which q_{95} and plasma normalized beta close to that required in ITER high-Q operation. Different from previous observations in the other machines, there is not only an upper density limit but also a lower one for accessing to ELM suppression.

Modelling results using the MARS-F code show that RMP with linear plasma response has a peak at intermediate plasma density and decays in both sides with increasing and decreasing density, which results in a minimal RMP field penetration threshold at intermediate plasma density. In this experiment, different densities result in different edge current profiles, which changes the local field line pitch, and hence, the eigenmode structure that causes a reduction of resonant field components in both low and high density cases. This makes field penetration be more difficult at both low and high density cases. The modelled window of strongest resonant spectrum taking into account plasma response in terms of [$\langle n_e \rangle$, q_{95}] agrees well with the observed ELM suppression window in EAST. The reason for loss of ELM suppression at low density at fixed q_{95} is due to the up-shift of the q_{95} window results from the change of edge bootstrap current.

Peeling-ballooning stability analysis using the ELITE code shows that plasmas gradually approach peeling stability boundary caused by increase of edge bootstrap current as the plasma density decreases, which is consistent with the observation that ELMs come back again in lower density plasmas for fixed q_{95}. PBMs are the most stable at intermediate plasma density, which is favorable for keeping ELM suppression state during the application of RMPs. The combined effects determine the RMP ELM suppression density window.

It is shown that linear modelling with full toroidal geometry can well predict the optimized RMPs for accessing to ELM suppression and reveals the important roles of pedestal current on ELM suppression, which need to be carefully considered in the application of high-n RMPs for ELM suppression. These findings provide a possible way to find optimized path that keep ELM suppression using high-n RMPs in scenario development for high-Q operation in ITER.

ACKNOWLEDGEMENTS

This work was supported by the National MCF Energy R&D Program of China under Grants No. 2024YFE03010000, and the Strategic Priority Research Program of Chinese Academy of Sciences under Grant No. XDB0790100. We thank the staff members at EAST (https://cstr.cn/31130.02.EAST), for providing technical support and assistance in data collection and analysis.

REFERENCES

REFERENCES

[1] T.E. Evans, *et al.*"Edge stability and transport control with resonant magnetic perturbations in collisionless tokamak plasmas," Nat. Phys **2**, 419–423 (2006).

[2] Y.M. Jeon, *et al.*, "Suppression of edge localized modes in high-confinement KSTAR plasmas by nonaxisymmetric magnetic perturbations," Phys. Rev. Lett. **109**, 035004 (2012).

[3] Y. Sun, *et al.*, "Nonlinear transition from mitigation to suppression of the edge localized mode with resonant magnetic perturbations in the EAST tokamak," Phys. Rev. Lett. **117**, 115001 (2016).

[4] W. Suttrop, *et al.*, "Experimental conditions to suppress edge localised modes by magnetic perturbations in the ASDEX upgrade tokamak," Nuclear Fusion **58**, 096031 (2018).

[5] H Zohm, "Edge localized modes (ELMs)," Plasma Phys. Control. Fusion **38**, 105 (1996).

[6] A. Loarte, *et al.*, "Characteristics of type I ELM energy and particle losses in existing devices and their extrapolation to ITER," Plasma Phys. Control. Fusion **45**, 1549 (2003).

[7] Y. Liang, *et al.*, "Active Control of Type-I Edge-Localized Modes with $n = 1$ Perturbation Fields in the JET Tokamak," Phys. Rev. Lett. **98**, 265004 (2007).

[8] A. Kirk, *et al.*, "Resonant magnetic perturbation experiments on MAST using external and internal coils for ELM control," Nuclear Fusion **50**, 034008 (2010).

[9] R. A. Moyer, *et al.*, "Validation of the model for elm suppression with 3d magnetic fields using low torque ITER baseline scenario discharges in DIII-D," Phys. Plasmas **24**, 102501 (2017).

[10] C. Paz-Soldan, *et al.*, "The effect of plasma shape and neutral beam mix on the rotation threshold for RMP-ELM suppression," Nucl. Fusion **59**, 056012 (2019).

[11] T.E. Evans, *et al.*, "Suppression of large Edge-Localized Modes in high-confinement DIII-D plasmas with a stochastic magnetic boundary," Phys. Rev. Lett. **92**, 235003 (2004).

[12] M.J. Lanctot, *et al.*, "Sustained suppression of type-I edge-localized modes with dominantly $n = 2$ magnetic fields in DIII-D," Nucl. Fusion **53**, 083019 (2013).

[13] Yongkyoon In, *et al.*, "Tamed stability and transport using controlled non-axisymmetric fields in KSTAR," Nucl. Fusion **59**, 056009 (2019).

[14] Y. Sun, *et al.*, "First demonstration of full ELM suppression in low input torque plasmas to support iter research plan using $n = 4$ RMP in EAST," Nucl. Fusion **61**, 106037 (2021).

[15] T.E. Evans, *et al.*, "RMP ELM suppression in DIII-D plasmas with ITER similar shapes and collisionalities," Nucl. Fusion **48**, 024002 (2008).

[16] Yueqiang Liu, *et al.*, "Modelling of plasma response to resonant magnetic perturbation fields in MAST and ITER," Nucl. Fusion **51**, 083002 (2011).

[17] Xu Yang, *et al.*, "Modelling of plasma response to 3D external magnetic field perturbations in EAST," Plasma Phys. Control. Fusion **58**, 114006 (2016).

[18] Yueqiang Liu, *et al.*, "ELM control with RMP: plasma response models and the role of edge peeling response," Plasma Phys. Control. Fusion **58**, 114005 (2016).

[19] Y. Sun, *et al.*, "Edge localized mode control using $n = 1$ resonant magnetic perturbation in the EAST tokamak," Nucl. Fusion **57**, 036007 (2017).

[20] R. Nazikian, *et al.*, in *Proc. 25th Int. Conf. on Fusion Energy (St Petersberg, Russian Federation, 13-18 October 2014)* (2014) pp. EX/1–1.

[21] W. Suttrop, *et al.*, "Experimental conditions to suppress edge localised modes by magnetic perturbations in the ASDEX Upgrade tokamak," Nucl. Fusion **58**, 096031 (2018).

[22] Q. M. Hu, *et al.*, "The density dependence of edge-localized-mode suppression and pump-out by resonant magnetic perturbations in the DIII-D tokamak," Phys. Plasmas **26**, 120702 (2019).

[23] Q. M. Hu, *et al.*, "Wide operational windows of edge-localized mode suppression by resonant magnetic perturbations in the DIII-D tokamak," Phys. Rev. Lett. **125**, 045001 (2020).

[24] Q.M. Hu, *et al.*, "The role of edge resonant magnetic perturbations in edge-localized-mode suppression and density pump-out in low-collisionality DIII-D plasmas," Nucl. Fusion **60**, 076001 (2020).

[25] Markus Markl, *et al.*, "Kinetic study of the bifurcation of resonant magnetic perturbations for edge localized mode suppression in ASDEX Upgrade," Nucl. Fusion **63**, 126007 (2023).

[26] Manni Jia, *et al.*, "Integrated ELM and divertor power flux control using RMPs with low input torque in EAST in support of the ITER research plan," Nucl. Fusion **61**, 106023 (2021).

[27] A. Loarte, *et al.*, "Progress on the application of ELM control schemes to ITER scenarios from the non-active phase to DT operation," Nucl. Fusion **54**, 033007 (2014).

[28] Hao Qu, *et al.*, "Q-band X-mode reflectometry and density profile reconstruction," Plasma Sci. Technol **17**, 985 (2015).

[29] H.Q. Liu, *et al.*, "Faraday-effect polarimeter-interferometer system for current density measurement on EAST," Rev. Sci. Instrum **85**, 11D405 (2014).

[30] Q. Zang, *et al.*, "Characteristics of edge pedestals in LHW and NBI heated H-mode plasmas on EAST,"

Nucl. Fusion **56**, 106003 (2016).

[31] Y.Y. Li, *et al.*, "Development of the charge exchange recombination spectroscopy and the beam emission spectroscopy on the EAST tokamak," Rev. Sci. Instrum **85**, 11E428 (2014).

[32] L.L. Lao, *et al.*, "Equilibrium analysis of current profiles in tokamaks," Nucl. Fusion **30**, 1035 (1990).

[33] G.Q. Li, *et al.*, "Kinetic equilibrium reconstruction on EAST tokamak," Plasma Phys. Control. Fusion **55**, 125008 (2013).

[34] Alexei Pankin, Douglas McCune, Robert Andre, Glenn Bateman, Arnold Kritz, "The tokamak Monte Carlo fast ion module NUBEAM in the national transport code collaboration library," Comput. Phys. Commun **159**, 157 (2004).

[35] O. Sauter, C. Angioni, Y. R. Lin-Liu, "Neoclassical conductivity and bootstrap current formulas for general axisymmetric equilibria and arbitrary collisionality regime," Phys. Plasmas **6**, 2834 (1999).

[36] O. Sauter, C. Angioni, Y. R. Lin-Liu, "Erratum: "neoclassical conductivity and bootstrap current formulas for general axisymmetric equilibria and arbitrary collisionality regime" [phys. plasmas 6, 2834 (1999)]," Phys. Plasmas **9**, 5140 (2002).

[37] Yueqiang Liu, A. Kirk, E. Nardon, "Full toroidal plasma response to externally applied nonaxisymmetric magnetic fields," Phys. Plasmas **17**, 122502 (2010).

[38] Pengcheng Xie, *et al.*, "Plasma response to resonant magnetic perturbations near rotation zero-crossing in low torque plasmas," Physics of Plasmas **28**, 092511 (2021).

[39] M. J. Lanctot, *et al.*, "Validation of the linear ideal magnetohydrodynamic model of three-dimensional tokamak equilibria," Phys. Plasmas **17**, 030701 (2010).

[40] A Kirk, *et al.*, "Magnetic perturbation experiments on MAST L- and H-mode plasmas using internal coils," Plasma Phys. Control. Fusion **53**, 065011 (2011).

[41] J. D. King, *et al.*, "Three-dimensional equilibria and island energy transport due to resonant magnetic perturbation edge localized mode suppression on DIII-D," Phys. Plasmas **22**, 112502 (2015).

[42] P.B. Snyder, *et al.*, "Edge localized modes and the pedestal: A model based on coupled peeling-ballooning modes," Phys. Plasmas **9**, 2037 (2002).

[43] O. Meneghini, *et al.*, "Integrated modeling applications for tokamak experiments with OMFIT," Nucl. Fusion **55**, 083008 (2015).

[44] T.H. Osborne, *et al.*, "Edge stability of stationary ELM-suppressed regimes on DIII-D," J. Phys.: Conf. Ser **123**, 012014 (2008).

[45] X.M. Wu, *et al.*, "Influence of $n = 4$ RMPs on pedestal structure and stability in EAST," Nucl. Fusion **65**, 076031 (2025).